DETECTING DEEP TECTONIC TREMOR IN TAIWAN USING

DENSE ARRAYS

A Thesis
Presented to
The Academic Faculty

by

Wei-Fang Sun

In Partial Fulfillment
of the Requirements for the Degree
Master of Science in the
School of Earth and Atmospheric Sciences

Georgia Institute of Technology
December, 2014

DETECTING DEEP TECTONIC TREMOR IN TAIWAN USING

DENSE ARRAY

Approved by:

Dr. Zhigang Peng, Advisor
School of Earth and Atmospheric Sciences
Georgia Institute of Technology

Dr. Andrew V. Newman
School of Earth and Atmospheric Sciences
Georgia Institute of Technology

Dr. Christian Huber
School of Earth and Atmospheric Sciences
Georgia Institute of Technology

Date Approved: July 28, 2014

ACKNOWLEDGEMENTS

TABLE OF CONTENTS

LIST OF TABLES

LIST OF FIGURES

SUMMARY

Deep tectonic tremor has been observed in major subduction zones, strike-slip faults, inland faulting systems, and arc-continent collision environments around the Pacific Rim. However, detailed space-time evolution of its source locations remains enigmatic because of difficulties in detecting and locating tremor accurately. In 2011, we installed two dense, small-aperture seismic arrays aiming to detect ambient tremor source beneath southern Central Range in Taiwan. We recorded continuous waveforms for a total of 134 days, including tremor triggered by the great 2011 Mw9.0 Tohoku earthquake. We use the broadband frequency-wavenumber beamforming and the moving-window grid-search methods to compute array parameters for detecting seismic signals. The obtained array parameters closely match both relocated local earthquakes and triggered tremor bursts located by an envelope cross-correlations method, indicating the robustness of our array technique. We identify tremor signals with coherent waveforms and deep incidence angles and detect tremor for 44 days among the 134-day study period. The total duration is 1,481-minute, which is 3-6 times more than that detected by the envelope cross-correlations method. In some cases, we observe rapid tremor migration with a speed at the order of 40-50 km/hour that is similar to the speed of fast tremor migration along-dip on narrow streaks in Japan and Cascadia. Our results suggest that dense array techniques are capable of capturing detailed spatiotemporal evolutions of tremor behaviors in southern Taiwan.

CHAPTER 1

INTRODUCTION

Deep tectonic tremor, also called non-volcanic tremor (NVT), has been observed at the subduction zones around the Pacific Rim (Beroza and Ide 2011; Peng and Gomberg 2010; and references therein). At strike-slip faults or inland faulting systems, tremor has been found along the San Andreas Fault (SAF) system in California (Gomberg *et al.* 2008; Nadeau and Dolenc 2005; Peng *et al.* 2009; Shelly *et al.* 2009; Shelly *et al.* 2011), the Alpine fault in the South Island of New Zealand (Wech *et al.* 2012), the Queen Charlotte Margin in western Canada (Aiken *et al.* 2013), the Oriente fault in Cuba (Peng *et al.* 2013), and at Kyushu and Kanto areas in Japan (Chao and Obara 2014). In the arc-continent collision environment in Taiwan, tremor is observed beneath the Central Range (Chao *et al.* 2012, 2013; Chao *et al.* 2014; Chuang *et al.* 2014; Idehara *et al.* 2014; Peng and Chao 2008; Tang *et al*. 2010, 2013). Different from regular earthquakes, deep tremor is recognized as non-impulsive, low-amplitude, and long-duration signal (Obara 2002), and often accompanied with slow-slip events (Rogers and Dragert 2003). Because most recent studies have shown that tremor activity mainly distribute along major fault interface and below the seismogenic zone where regular earthquakes occur (Ghosh *et al.* 2012; Shelly and Hardebeck 2010), a systematic study of tremor can help to better understand necessary conditions related to tremor occurrence and fault mechanics at the bottom of the seismogenic layer.

The Island of Taiwan (Figure 1) is located at the boundary between the Eurasia and the Philippine Sea plates with two subduction systems – the Ryukyu Trench in the northeast and the Manila Trench in the southwest (Tsai 1986; Angelier *et al.* 2001) with convergent rates 5 cm yr^{-1} (Nishizawa *et al.* 2009) and 2-10 cm yr^{-1} (Galgana *et al.* 2007),

respectively. In between of the north-dipping subduction zone to the northeast and the east-dipping subduction zone to the southwest of the island, the Luzon volcanic arc collides into the Chinese continental margin with a converge rate of about 8 cm yr^{-1} (Yu *et al.* 1997). Such collision creates the Central Range (the green area in Figure 1 and HR, BR, and ECR in Figure 2), the backbone of the island.

Peng and Chao (2008) first identified triggered tremor beneath the Central Range following the 2001 Mw7.9 Kunlun earthquake in northern Tibet. Subsequent tremor studies mainly focus on low-frequency earthquakes (Tang *et al.* 2010; Tang *et al.* 2013) and both triggered (Chao *et al.* 2012; Chao *et al.* 2013) and ambient tremor (Chao *et al.* 2014; Chuang *et al.* 2014; Idehara *et al.* 2014) in southern Central Range. Those studies utilized seismic data from two permanent seismic networks: the Broadband Array in Taiwan for Seismology (BATS) operated by the Institute of Earth Sciences (IES) in Academia Sinica (Kao *et al.* 1998) and the short-period CWB Seismic Network (CWBSN) and the CWB Broadband Seismic Network operated by the Central Weather Bureau (CWB) (Shin *et al.* 2013), and one temporally deployed linear array, the TAIGER (Taiwan Integrated GEodynamic Research) (Wu *et al.* 2014; Huang *et al.* 2013). The spatiotemporal distribution of tremor has been mapped (Chao *et al.* 2014; Chuang *et al.* 2014) using envelope cross-correlation (WECC) methods (Wech and Creager 2008; Wech 2010). However, due to the sparse station distribution of the BATS and CWB networks, and elevated background noises in the Island of Taiwan, obtaining a complete list of tremor activity is difficult.

High-quality seismic data recorded by dense small-aperture seismic arrays have been used to increase tremor detectability and to obtain high-resolution tremor location in

Cascadia (Ghosh *et al.* 2009; Ghosh *et al.* 2010; Ghosh *et al.* 2012; La Rocca *et al.* 2008) and the SAF (Fletcher and Baker 2010; Ryberg *et al.* 2010; Ghosh 2014). In Cascadia, when the multibeam-backprojection method is applied to the array data (Ghosh *et al.* 2012), nearly continuous tremor activities were detected. The array-based results provide more details of spatiotemporal characteristics when comparing with the network-based methods, such as the envelope WECC method (e.g., Wech and Creager 2008), the source-scanning algorithm (Kao *et al.* 2006), and the waveform matching technique (Shelly *et al.* 2007a).

To better understand tremor behaviors in southern Central Range, we installed two temporal dense seismic arrays (Figure 2) in the first six months of 2011. This deployment was fortunate because it captured triggered tremor following the 2011/03/11 Mw9.0 Tohoku earthquake (Chao *et al.* 2013) and many background tremor episodes. In this study, we combine the broadband frequency-wavenumber (BBFK) beamforming (Goldstein *et al.* 2003; Nawab *et al.* 1985) and the moving-window grid-search (MWGS) (Fletcher *et al.* 2006; Fletcher and Baker 2010; Frankel *et al.* 1991) methods to detect weak tremor signals. We also use triggered tremor bursts and local earthquakes to test the detection ability of each array.

In the following chapters, we first describe the array deployment and the array-processing methods. In chapters 3 and 4, we outline the tests for detection abilities of the two arrays and apply both methods to the entire data set to obtain the ambient tremor catalog. Finally, we compare our detection results with the other two tremor catalogs (Chao *et al.* 2014; Chuang *et al.* 2014) and discuss the implications.
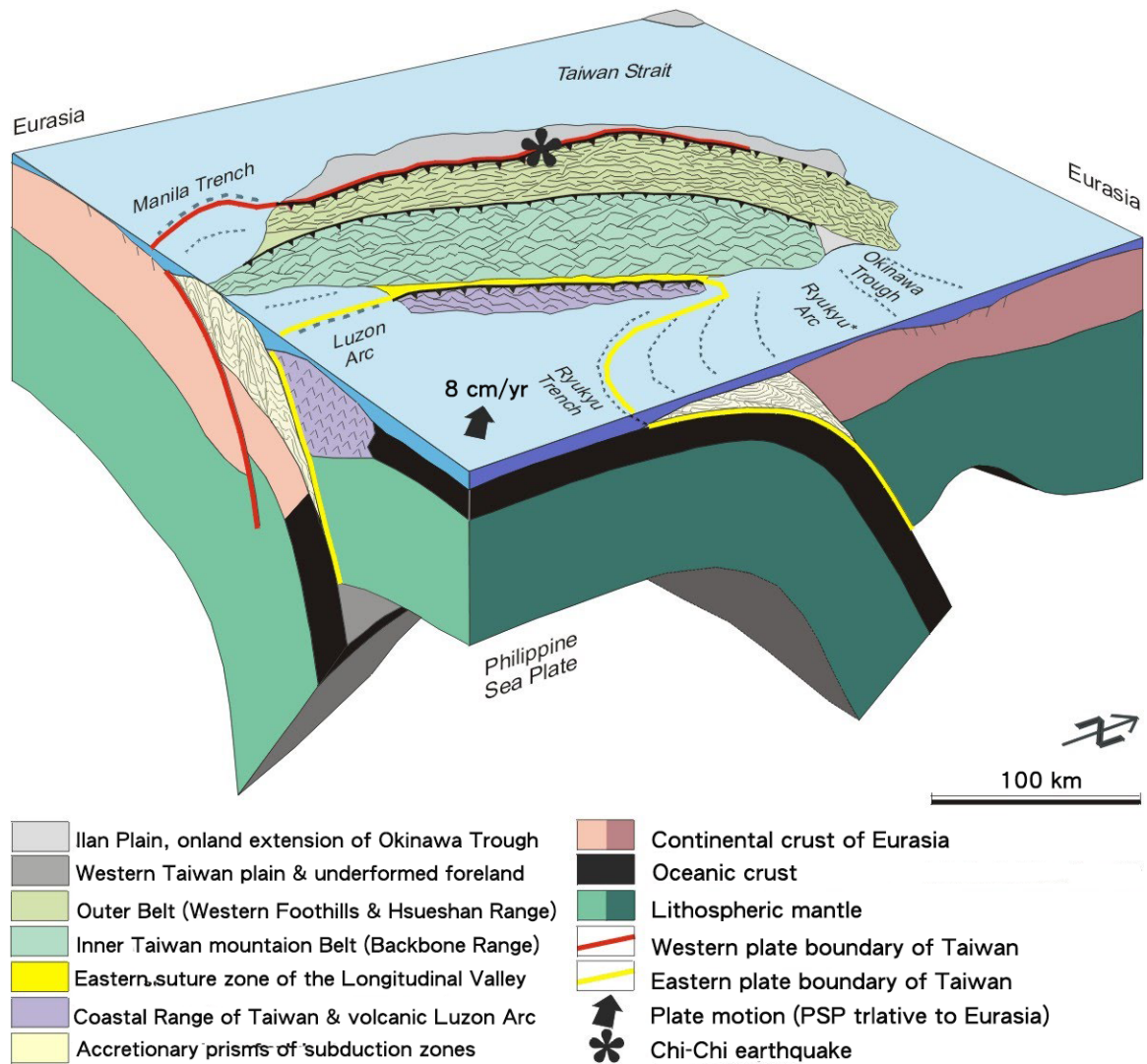
Figure 1. Tectonic setting in Taiwan. Modified from Angelier *et al.* (2001).
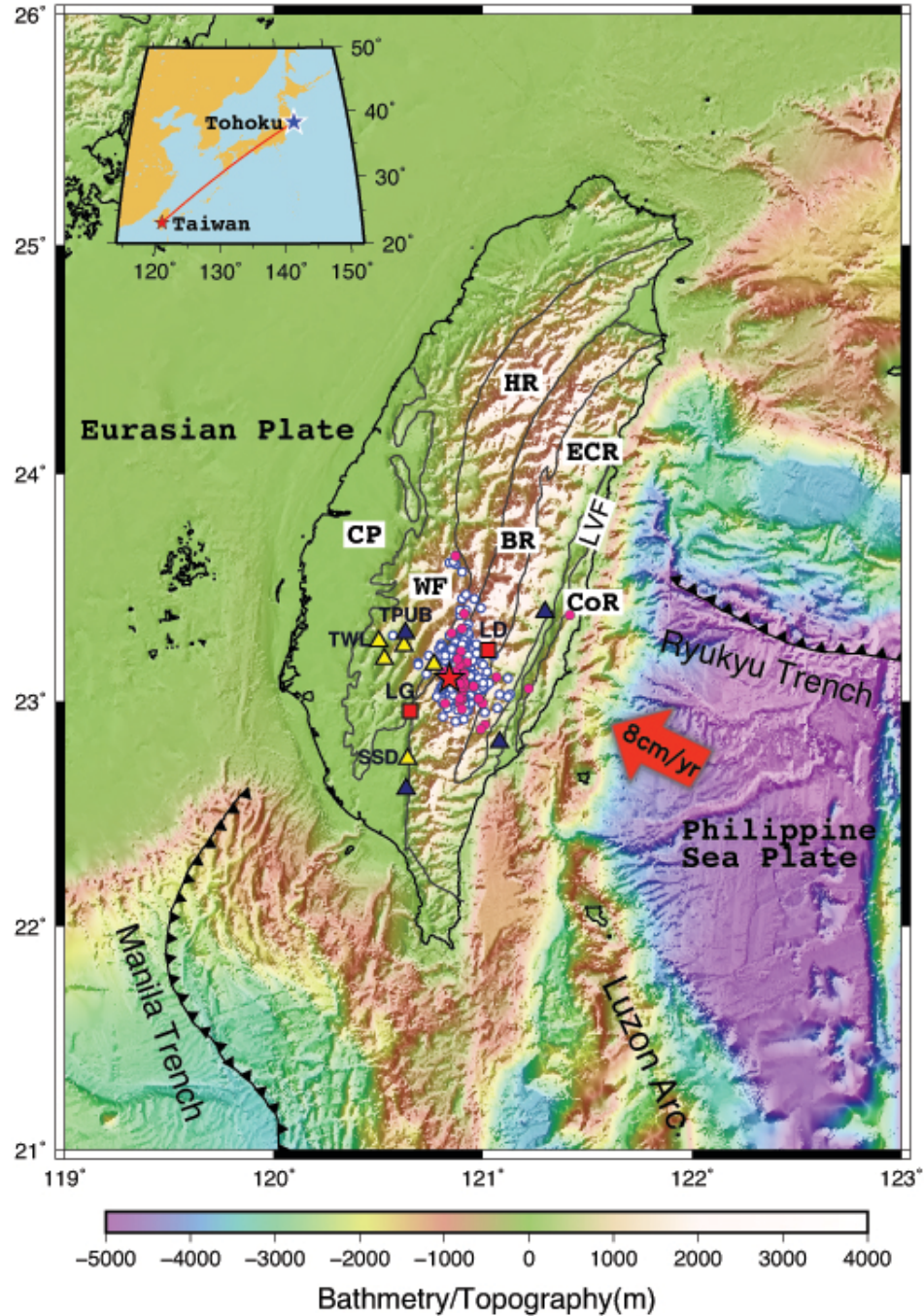
Figure 2. Map of study region in Taiwan. The average triggered tremor source following the 2011 Mw9.0 Tohoku mainshock (Chao *et al.* 2013) is marked as red star. The red squares indicate the locations of the LG and LD arrays. The open blue and solid magenta circles are ambient tremor sources detected by Chao *et al.* (2014) and Chuang *et al.* (2014), respectively. The blue and yellow triangles are the adjacent, permanent BATS and CWBSN stations, respectively. Geological provinces: CP-Coastal Plain, WF-Western Foothill, HR-Hsueshan Range, BR-Backbone Range or Tananao Schist complex, ECR-East Central Range, LVF- Longitudinal Valley Fault, and CoR-Costal Range. The red arrow indicates the convergent direction of two plates.

CHAPTER 2

DATA AND ANALYSIS PROCEDURE

Aiming to evaluate triggered tremor sources (Peng and Chao, 2008; Chao *et al.* 2009), in 2011 we installed two dense small-aperture seismic arrays at the southwest and northeast of the active tremor source in Liouguei (LG array) and Lidao (LD array) areas, respectively (Figure 2). Each array includes 36 short-period vertical-channel GS-11D sensors with 4.5Hz natural frequency. We recorded continuous ground velocity data at 100 samples per second. The instruments were deployed in areas of 700 m by 900 m for the LG array (Figure 3a; Table A1) and 300 m by 650 m for the LD array (Figure 3a; Table A2) on a relatively flat part of each mountain area. We used the TEXAN data loggers to record seismic data (Figure 3c). The original design of TEXAN contains two D Alkaline batteries, which can only last for about 5-7 days for continuous recording. We used an external wire designed for TEXAN to connect to the 120A/12V car battery (Figure 3c), so that the TEXAN could record continuously for about 20-22 days before batteries replacement. Data for some stations is available back to January 1, 2011. However, the recording is mostly complete for a total of 134 days from February 12 to July 7, 2011. Among them, we did not have recordings for 12 days (2011 Julian day 62, 63, 84, 85, 105, 106, 126, 127, 147, 148, 168, and 169) due to instrument repair/battery replacement about every 20 days.

In this study, we detected tremor by two array-processing techniques, the broadband frequency-wavenumber (BBFK) beamforming (Goldstein *et al.* 2003; Nawab *et al.* 1985) and the moving-window grid-search (MWGS) (Fletcher *et al.* 2006; Fletcher

and Baker 2010; Frankel *et al.* 1991) methods. Both methods require a plane wave assumption so that the differential travel time of the plane wave front is due to a specific slowness and back azimuth. We corrected for such time shifts with the best-fitting slowness and back azimuth and then stacked all signals (i.e., delay-and-sum) to obtain an array-averaged recording (Fletcher *et al.* 2006; Ghosh *et al.* 2009; Rost and Thomas 2002).

For the BBFK method, the peak frequency-wavenumber of the dominant signals is calculated in the frequency domain. The wavenumber k (1/km) of the plane wave is calculated by the equation $k = f \times p$, where f (Hz) is frequency and p (s/km) is horizontal slowness. The wavenumber and slowness were obtained from the maximum amplitude of the wavenumber spectrum (Helffrich *et al.* 2013). We used the built-in command of 'BBFK' in the Seismic Analysis Code (SAC) to compute broadband frequency-wavenumber spectra (Goldstein *et al.* 2003; Nawab *et al.* 1985).

For the MWGS method, the peak cross-correlation coefficient (CC) values of time-corrected waveforms due to slowness vectors are calculated in the time domain (Fletcher *et al.* 2006). We developed a MATLAB-based technique with the following steps. First we calculated the time correction as a function of slowness of seismograms for all stations in both array. Next we obtained the CC values as a function of slowness by averaging correlation functions of all the individual station pair. The peak CC value corresponds to the best-fitting azimuth and apparent velocity for signals in a specific time window (Fletcher *et al.* 2006).

For tremor detection in this study, we first filtered the seismic data in the frequency range of 5-20 Hz. This range is slightly higher than the typical frequency range

of 1-10 Hz for tremor studies (Obara 2002). We chose 5-20 Hz mainly because the instrument corner frequency is 4.5 Hz. In addition, the tight array allows us to include higher frequencies in this study. For the BBFK method, we used BBFK in SAC to compute broadband frequency-wavenumber spectra and then obtained the best-fitting back-azimuth and wavenumber for every two-minute time window with a 50% overlapping (i.e., one-minute shift each time), the same time window setting as in Ghosh *et al.* (2010). For the MWGS method, we used the 20-second non-overlapping sliding window and searched for the best-fitting back-azimuth and apparent velocity with the maximum CC value. Here a smaller window size is used to follow the time window setting in Fletcher and Baker (2010).

Next, we combined the parameters obtained by BBFK and MWGS and band-pass-filtered envelope functions to visually identify tremor events. The criteria for eligible tremor detections are: (1) the detected duration time is longer than 3 minutes and the array envelope function are coherent among nearby permanent and temporary seismic stations in each array (Figure 2 and Figure 3); (2) back-azimuth obtained by both methods are consistent within 30° due to the relative position between the arrays and tremor sources (Figure 2); (3) the wavenumber obtained from BBFK is ≤ 1.5 (cycle/km), which implies that the seismic energy has a steep incidence angle; (4) the waveform CC values observed from MWGS is ≥ 0.02. The choices of these parameters are empirical, but with a common goal to detect tremor signals with stable azimuth and deep origin. In addition, we removed the detections of local and distant earthquakes by comparing our results with the local CWB and the global Advanced National Seismic System (ANSS) earthquake catalogs.
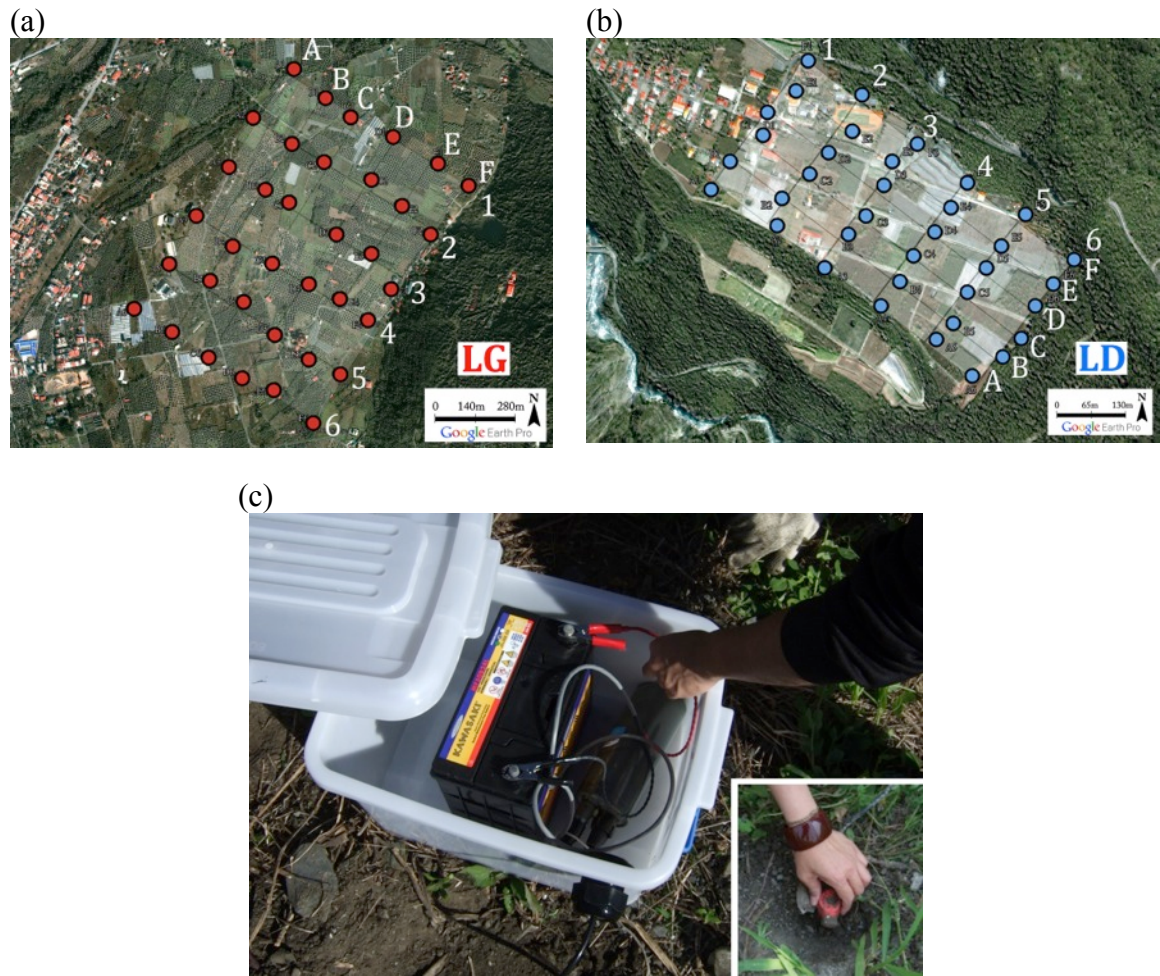
Figure 3. Configurations of both arrays and instrument setting. (a) The configuration and station locations (red dots) of the LG array in a grid of 140 by 180 meters. (b) The configuration and station locations (blue dots) of the LD array in a grid of 65 by 130 meters. (c) Instrument setting: the data logger (TEXAN) connects to a car battery in the box and the inset shows the vertical-channel GS-11D sensor (geophone) with a 4.5 Hz natural frequency.

CHAPTER 3

ROBUSTNESS TEST WITH LOCAL EARTHQUAKES

AND TRIGGERED TREMOR

To evaluate the robustness of our methods, we selected 111 adjacent earthquakes to test the detection ability by using the MWGS method with some adjustment in the parameters suitable for detecting earthquakes. Those relocated earthquakes (Wu *et al.* 2008) are one month before and after the 2011 Mw9.0 Tohoku mainshock with local magnitude M_L between 1.0 and 3.9, and the epicenter distances are less than 53 km to each array. Specifically, we manually picked the *S* arrival and used a 0.3~0.4s time widow (Figure 4c and 4d) to include first few cycles of *S*-wave of each earthquake to obtain the MWGS parameters. According to the back-azimuth differences between the relocated catalogs (Wu *et al.* 2008) and obtained back-azimuths by MWGS among the 111 local earthquakes, the LG array provides more accurate detections for 104 of them (94%) agree within 20° (Figure 4a). In comparison, 94 back-azimuth solutions (85%) were more than 20° for the LD array (Figure 4b). A detailed examination of waveforms recorded at the LD array also revealed possible time shifts at some stations (e.g. LDA6, LDC6, and LDD6) after accounting for the slowness and incidence angle (Figure 4d). This indicates either complicated local site conditions or timing errors in these stations.

Next, we applied both the BBFK and MWGS methods to detect triggered tremor following the 2011 Tohoku earthquake. Both the LG (Figure 5a) and the LD (Figure 5b) arrays recorded nine clear, triggered tremor bursts during the passing surface waves of the Tohoku mainshock. As shown in Figures 6 and 7 (and also Table 1), the back-

azimuths obtained by the BBFK with only the LG array match well with the burst locations from the envelope cross-correlation (Chao *et al.* 2013) and the WECC (Wech and Creager 2008; Wech 2010) methods.

These comparisons indicate that our array technique is robust and can be used to detect tremor episodes in Taiwan. Because of aforementioned issues at the LD array, in the following sections we only present results by applying both techniques to the LG array.
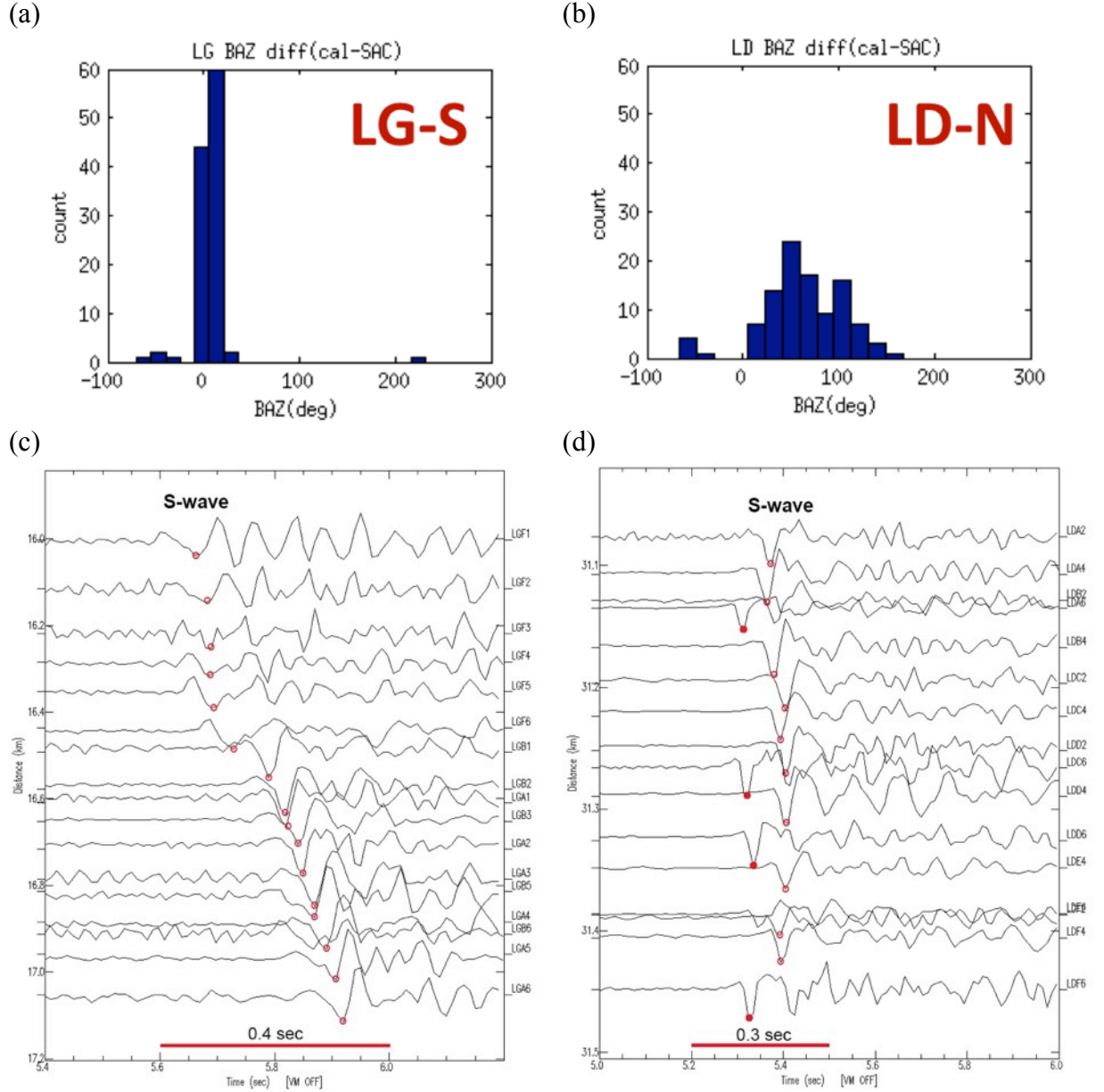
Figure 4. MWGS test with 111 local earthquakes. (a) and (b) Histograms of back-azimuth-difference obtained by Wu *et al.* (2008) and the MWGS method of the LG and the LD arrays, respectively. (c) and (d) Record-section of the epicenter distances among selected stations of the LG and the LD arrays, respectively, for one of the selected local earthquakes. Stations are identified at right. Red, open circles indicate S-wave arrivals and red line the time-windows for the MWGS method. In LD array (d), the arrivals among 4 stations (red, solid circles) – LDA6, LDC6, LDD6, and LDF6 – did not align to the relationship between epicenter distance and arrival time.
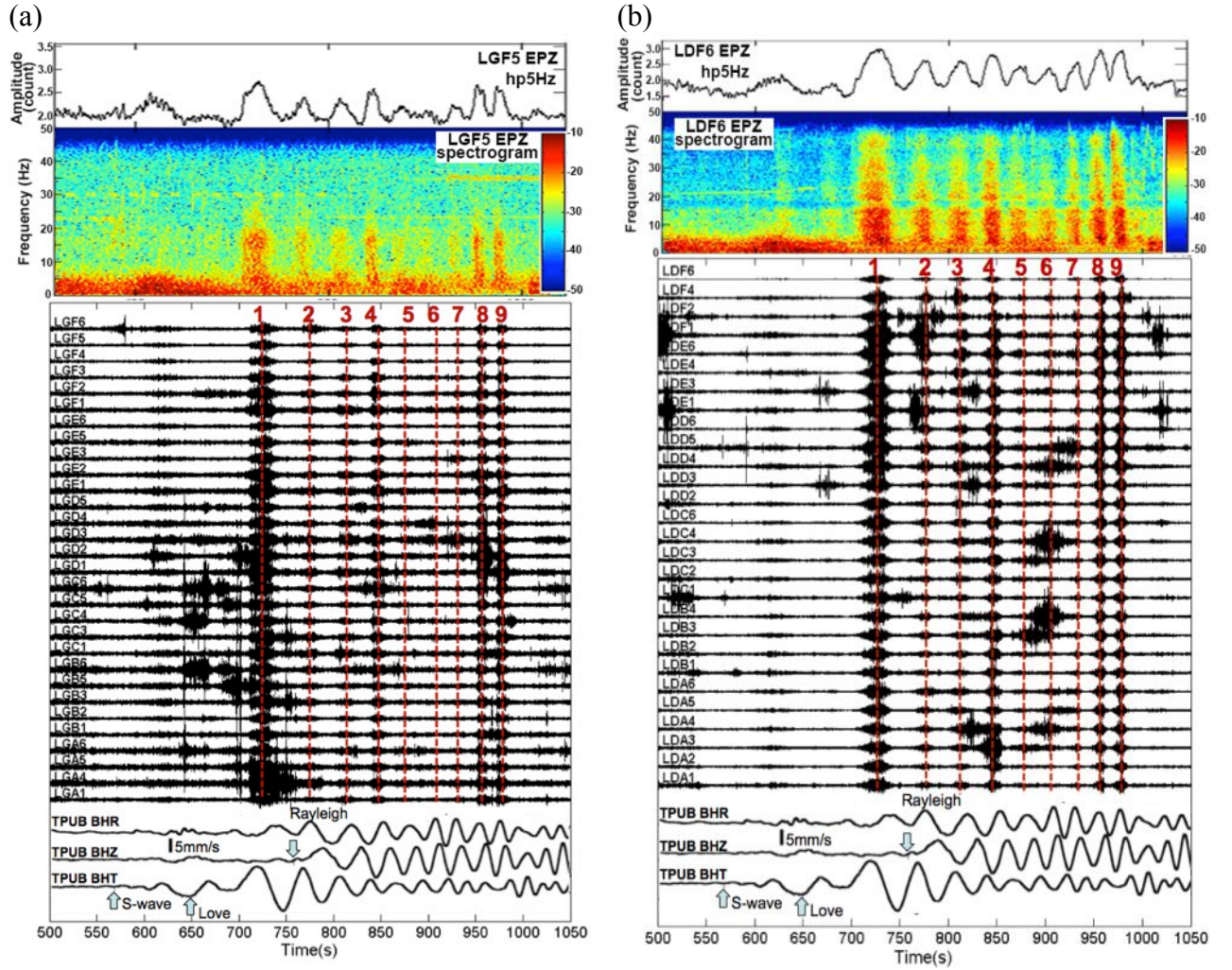
Figure 5. Deep tremor triggered by the 2011 Mw9.0 Tohoku earthquake recorded at the LG (a) and the LD (b) arrays. From top to bottom: the 5-Hz-high-pass envelope function (upper panel), spectrogram (middle panel), and the 5–20 Hz band-pass filtered seismograms (lower panel) recorded nine tremor bursts triggered by the Tohoku mainshock.
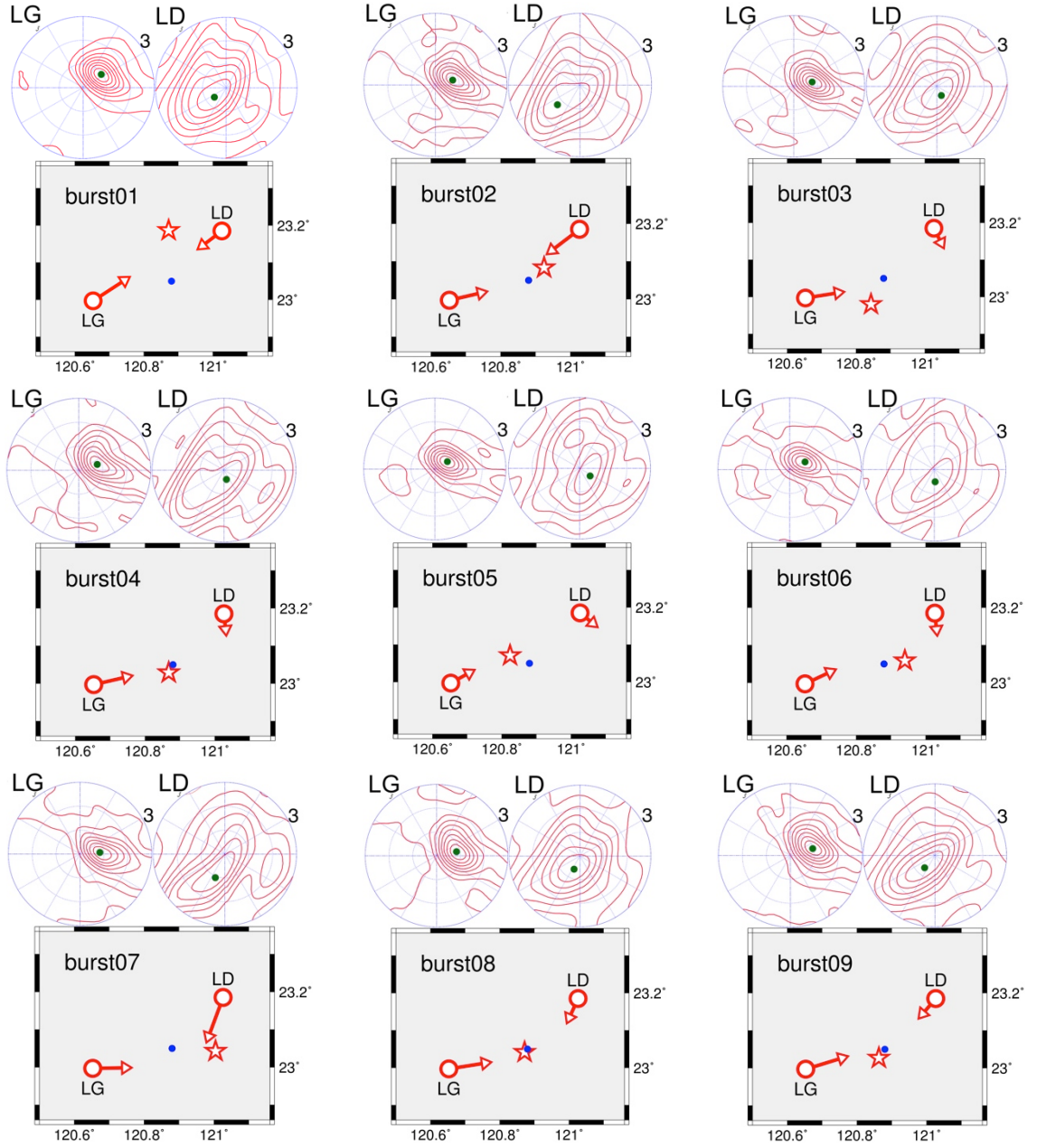
Figure 6. BBFK results for nine tremor bursts triggered by the Tohoku mainshock. In each panel, the contour plot on the top denotes the distribution of FK amplitude (beam power) as a function of back-azimuth (angle) and wavenumber (radius), and the location of the FK peak (green dot) marks the best solution of back-azimuth and wavenumber. In the lower panel, red open circles indicate the locations of the LG and the LD arrays, and the direction and length of each red arrow represent the back-azimuth and the wavenumber, respectively. The red star and blue dot are the locations of each tremor burst and the average tremor source, respectively, determined by the envelope cross-correlations (WECC) method (Wech and Creager 2008).
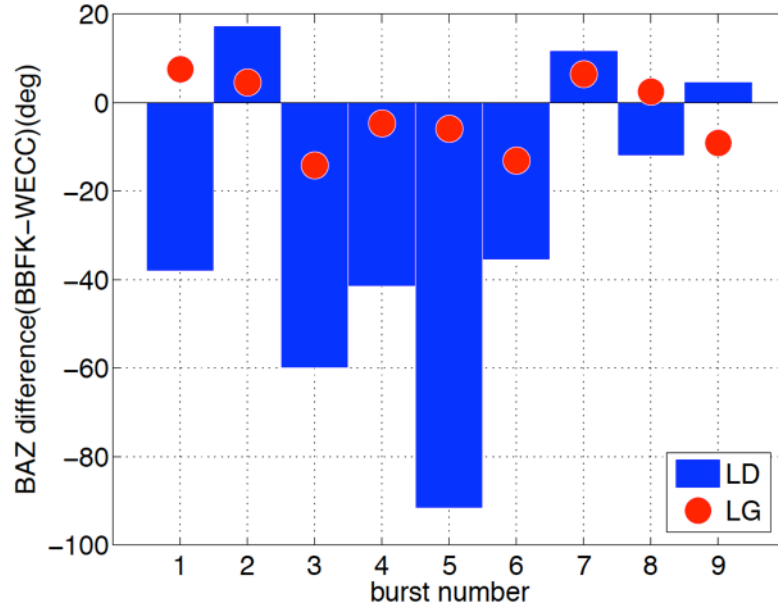
Figure 7. Back-azimuth (BAZ) differences between the BBFK and the WECC methods among the nine triggered tremor bursts for both arrays.

Table 1. Parameters of nine triggered tremor bursts

#	Longitude	Latitude	BAZ*(°) – LG array			BAZ*(°) – LD array		
			WECC	BBFK	ΔBAZ	WECC	BBFK	ΔBAZ
1	120.8718	23.1867	49.10	56.63	7.5	270.71	232.60	-38.1
2	120.9242	23.0835	72.32	76.85	4.5	215.34	232.60	17.3
3	120.8432	22.9800	95.10	80.90	-14.2	213.67	153.70	-60.0
4	120.8676	23.0288	81.58	76.85	-4.7	215.48	173.90	-41.6
5	120.8241	23.0711	66.61	60.67	-5.9	221.07	129.40	-91.7
6	120.9400	23.0588	77.86	64.72	-13.1	209.43	173.90	-35.5
7	121.0045	23.0429	82.56	88.99	6.4	188.56	200.20	11.6
8	120.8715	23.0418	78.42	80.90	2.5	216.28	204.30	-12.0
9	120.8629	23.0267	81.95	72.81	-9.1	215.69	220.40	4.7

*BAZ: Back-azimuth

CHAPTER 4

AMBIENT TREMOR DETECTION

Following the procedure to identify tremor mentioned in chapter 2, we apply it to detect ambient tremor for the entire time period. Figure 8 shows an example of ambient tremor detected on May 31st, 2011. Between 18:27 and 19:10 UTC, we observed a clear reduction in the wavenumber, indicating that the seismic signals have steep incidence angles during this time period. In the mean time, the back-azimuths measured from both BBFK and MWGS are stable, with mean values of 83° and 71°, respectively. The coherent tremor signals were also recorded by nearby BATS station TPUB and CWBSN station WTP (Figure 8a). Finally, this tremor episode was also detected by other recent studies (Chao *et al.* 2014; Chuang *et al.* 2014), and the obtained back-azimuths are comparable. Figure 9 shows an example of ambient tremor events only detected by this study. The tremor episodes that were not detected by the other two catalogs are generally weaker with shorter durations, which would partially explain why they were not detected by the standard WECC method (Figure 10).

Radiated seismic energy of an earthquake can be computed by integrating radiated energy flux in velocity-squared seismograms (Boatwright and Choy 1986). For comparing equivalent radiated seismic energy among triggered and ambient tremor, we simply sum the square of instrument-corrected velocity after high-pass filtered by 5Hz within individual tremor windows recorded by the BATS station TPUB. We then normalize it by the value of triggered tremor following the 2011 Tohoku mainshock. We use such normalization to remove potential distance/attenuation effect (by assuming that

triggered tremor originated from the same places of ambient tremor), and to compare the radiated energy between triggered and ambient tremor. Figure 10a shows that the normalized equivalent radiate energy (NERE) of triggered tremor is 1-3 orders more than that of ambient tremor. In addition, it appears that our method can detect tremor with weaker radiated energy than that detected by the other two WECC methods. After divided the NERE by duration of individual tremor episodes, we obtain the NERE rate. As shown in Figure 10b and 10c, tremor detected only by our method is generally shorter in duration (Figure 10b) and weaker in NERE rate and amplitude (Figure 10c).

Figure 11 shows a comparison among three different tremor catalogs during our deployment period. By using the LG array data, we identified 44 days containing at least one tremor episode among the 134-day period. The total duration is 1,481 minutes, and the average duration is 17 minutes (Table A3). The total tremor duration detected by our array method is 6 times more than that detected by Chao *et al.* (2014) (27 days/239 minutes) and 3 times more than that detected by Chuang *et al.* (2014) (21 days/450 minutes). Overall, the tremor detected by the BBFK and MWGS method are similar to other two catalogs in time, except that our catalog shows nearly continuous tremor activities after Julian day 176 (Figure 11). Interestingly, there was no tremor activity reported by three different studies (Chao *et al.* 2014; Chuang *et al.* 2014; this study) in the 10-day period following the 2011 Mw9.0 Tohoku earthquake and tremor rate returned back to previous recurrence cycle after 20 days (Figures 10 and 11).

Figure 12 shows a summary of back-azimuths and wavenumbers for tremor detections and all time windows analyzed by the BBFK method. Since the LG array was located at the southwestern side of tremor source regions, the back-azimuths for all

observed tremor range from N45^{o}E to N90^{o}E (Figure 12a). The tremor signal is barely visible at all during the entire time windows and the majority of seismic sources come from between N60^{o}E to S (Figure 12b) with wavenumber equals to 3 cycles/km. Due to the shallow incidence angles the likely sources are either shallow earthquakes from the eastern Longitudinal Valley Fault (LVF in Figure 2) or more likely background noises.

Among those 86 detected tremor events, some of them show migration behavior and the migration directions can be either southward or northward. For example, in Figure 8, tremor sources concentrate in the area with back-azimuths of ~85° between 18:36 and 19:00 UTC, and then move northward to the area with back-azimuths of ~55° between 19:00 and 19:10 UTC. Because we cannot obtain the absolute location of tremor source by using a single array, we use the tremor locations determined by Chao *et al.* (2014) to estimate the migration speed. A total of eight tremor events, which are both detected by Chao *et al.* (2014) and this study, show possible migration behaviors (Table 2). The average migration speed is ~110 km/hour (2,722 km/day), similar to that observed in other regions (Ghosh *et al.* 2009; Fletcher and Baker 2010).

2011-151
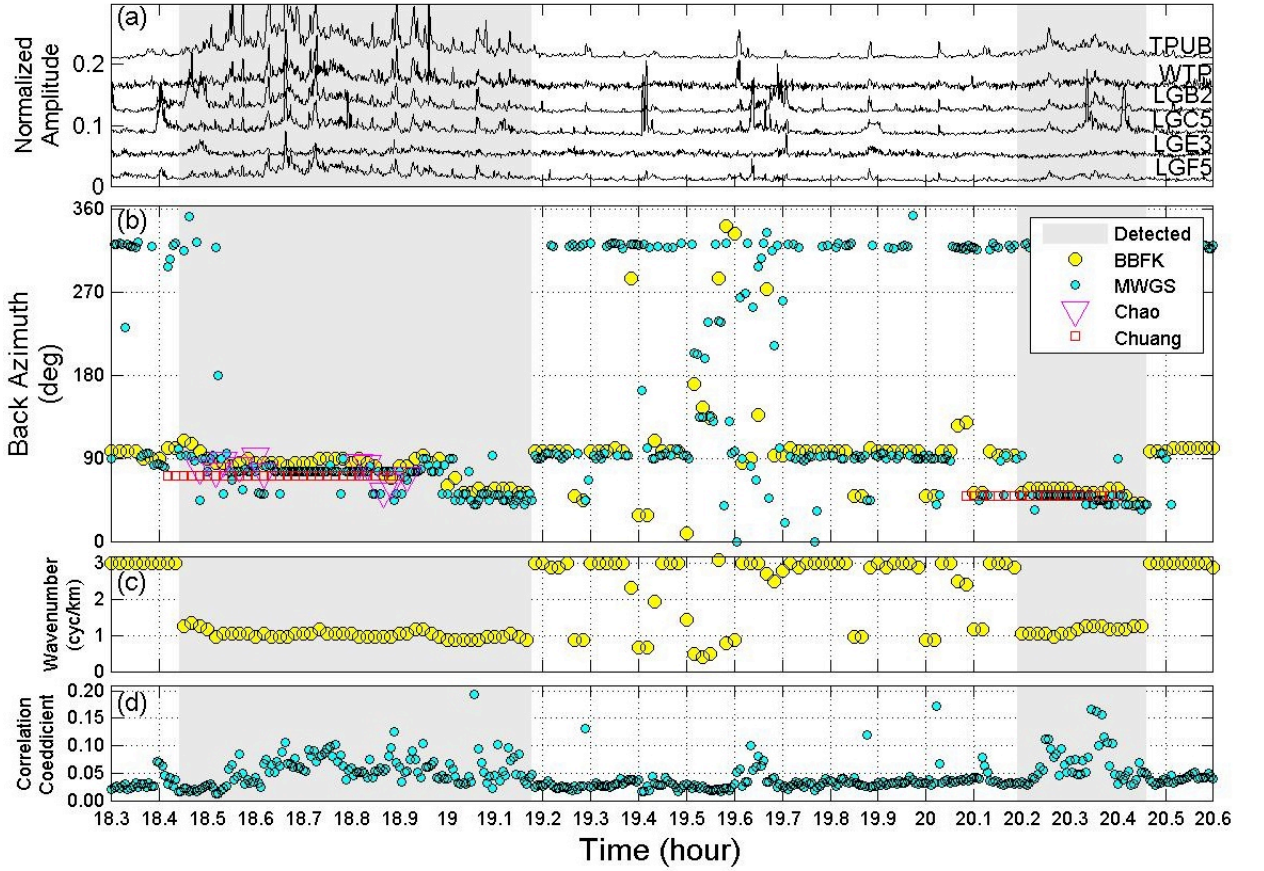
Figure 8. An example of ambient tremor detected by three methods. Panels (a-d) show normalized envelope function, back-azimuth, wavenumber and correlation coefficient versus UTC time on 2011 Julian day 151. The gray areas mark the tremor period identified by the combined BBFK-MWGS method and visual inspection. Other symbols and notations are marked in the legend.
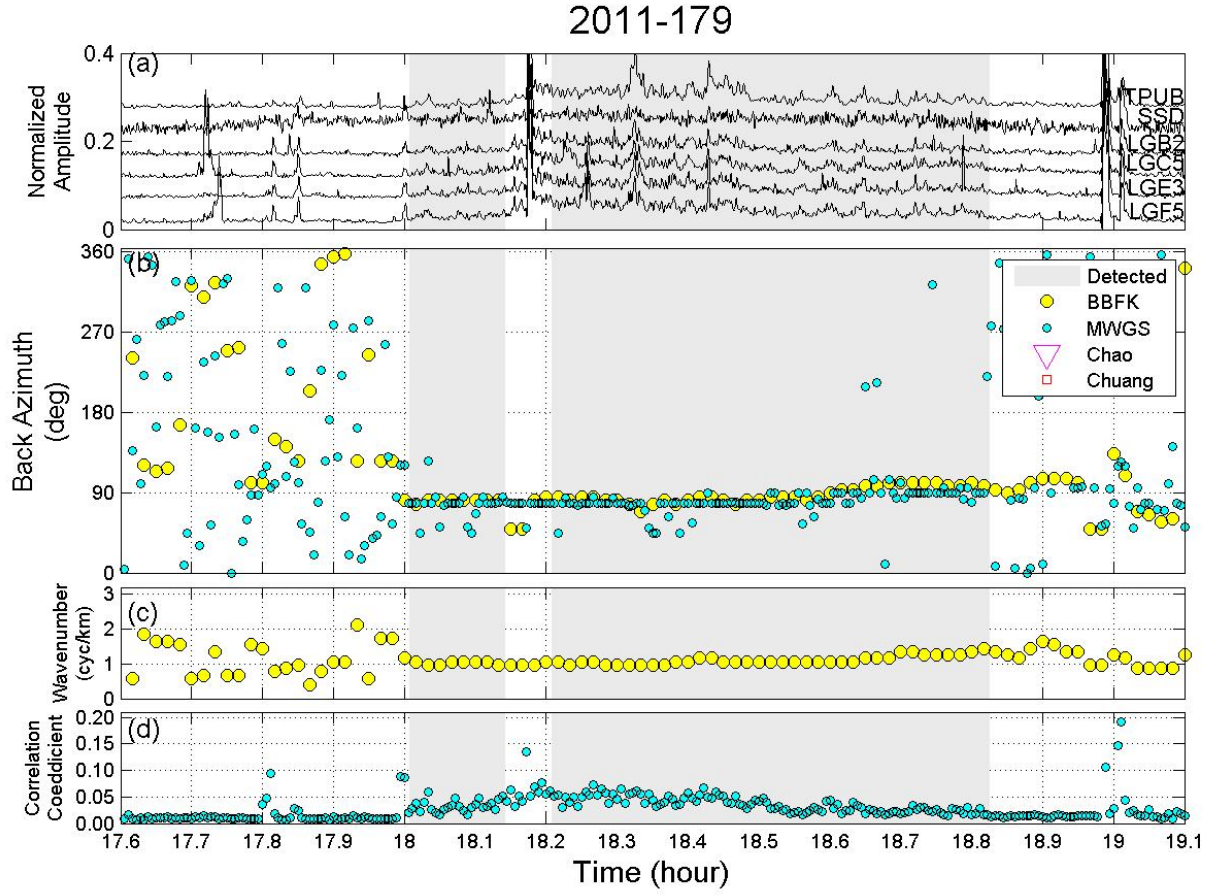
Figure 9. An example of ambient tremor detected only by our combined BBFK-MWGS method (gray area) in 2011 Julian day 179. Other notations are the same as in Figure 8.
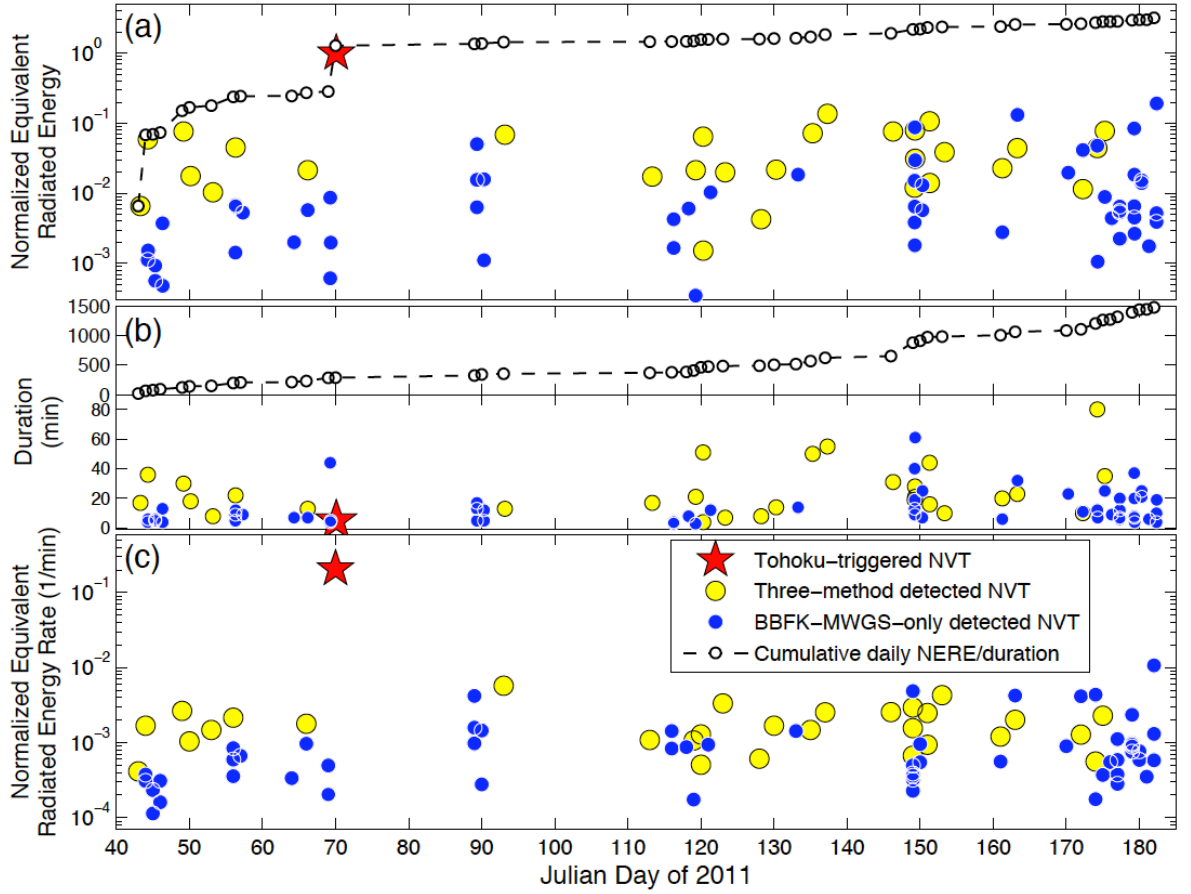
Figure 10. Normalized equivalent radiated energy and duration of detected tremor from three methods. The red starts denote the triggered tremor following the 2011 Tohoku surface waves; yellow and blue dots indicate ambient tremor detected by the two WECC and our BBFK-MWGS methods and by only our BBFK-MWGS method, respectively. (a) Normalized equivalent radiate energy of individual tremor episodes and cumulative, daily, radiated energy (open black circles and dashed line). (b) Duration of individual tremor episodes and cumulative daily duration (open black circles and dashed line). (c) Normalized equivalent radiate energy rate.
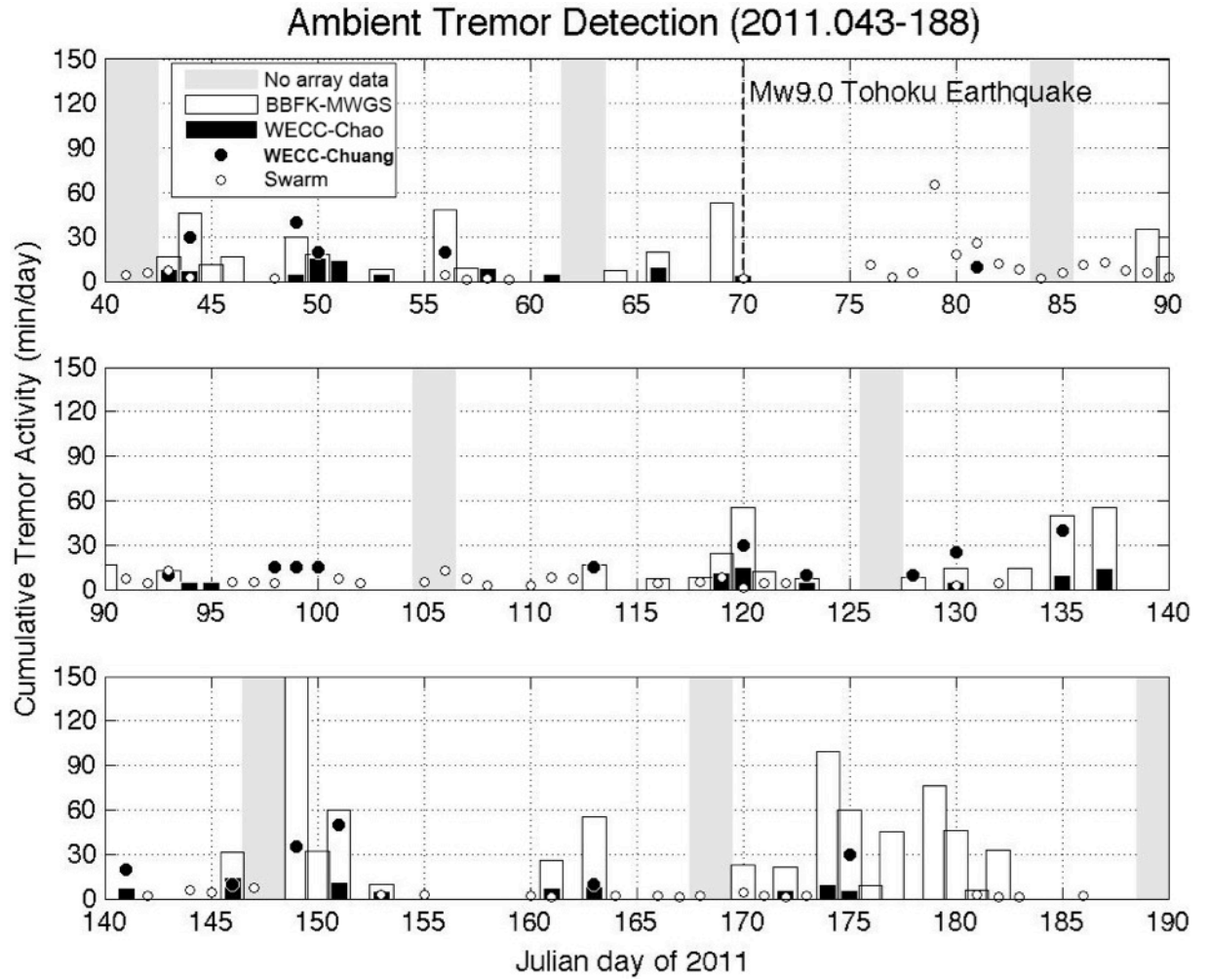
Figure 11. Daily tremor activity obtained in three studies: Combined BBFK-MWGS from this study (open histograms), WECC-Chao by Chao *et al.* (2014) (black histograms), and WECC-Chuang by Chuang *et al.* (2014) (solid circles). The open circles indicate daily accumulative swarm activity in the adjacent area (Wei Peng, personal communication, 2013). The gray areas mark those days without array data, and the dashed line mark the occurrence time of the 2011 Mw9.0 Tohoku earthquake.
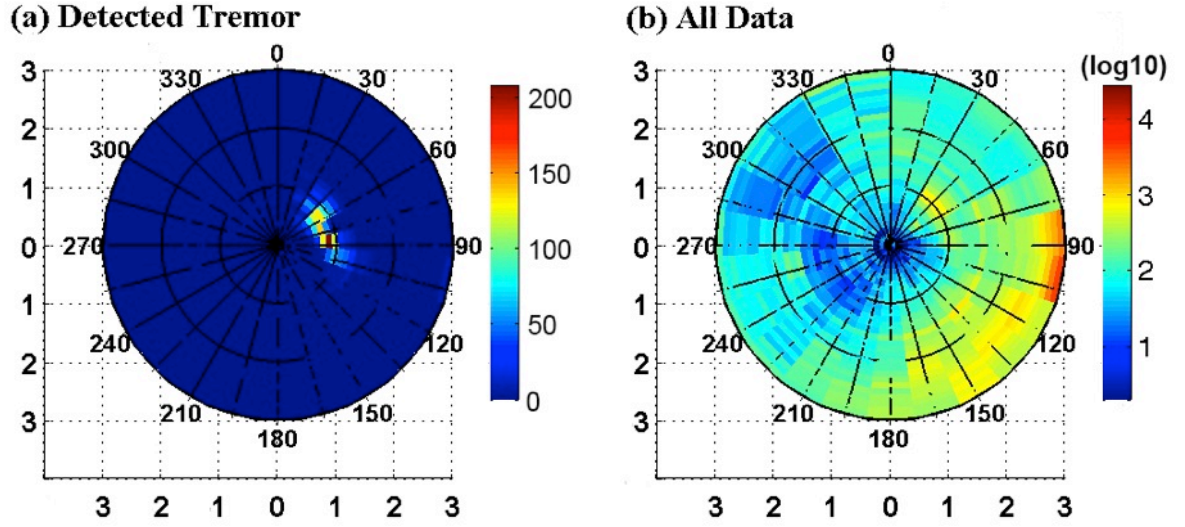
Figure 12. The distributions of back-azimuth (angle) and wavenumber (radius, cycles/km) of the BBFK method at the LG array for the detected tremor (a) and all time windows (b).

Table 2. Parameters for eight migrating tremor events. The event number (#) is the same as in Table A3 for the complete catalog of detected tremor by the LG array.

#	Julian Day	Start Hour	Start Min	End Hour	End Min	Duration (min)	Mean BBFK BAZ* (°)	Migration Direction	Migration Speed (km/s)
3	44	19	27	20	2	36	79.4	North	0.035
11	53	13	22	13	29	8	67.1	North	0.066
38	123	20	14	20	20	7	31.3	South	0.021
42	135	17	43	18	32	50	82.5	South	0.012
44	146	18	22	18	52	31	74.1	North	0.028
56	151	18	27	19	10	44	82.5	North	0.020
67	174	15	50	17	9	80	65.6	South	0.042
69	175	16	51	17	25	35	64.7	North	0.028

*BAZ: Back-azimuth

CHAPTER 5

DISCUSSION AND CONCLUSIONS

In this study we conducted a systematic detection of ambient tremor in southern Taiwan based on temporally deployed seismic arrays. The obtained tremor durations are 3-6 times greater than those detected based on permanent stations (Chao *et al.* 2014; Chuang *et al.* 2014). This is consistent with similar findings in Cascadia (Ghosh *et al.* 2009; Ghosh *et al.* 2010; Ghosh *et al.* 2012), suggesting that array techniques have higher detection capabilities than traditional envelope cross-correlation techniques (Wech *et al.* 2008). Unfortunately, we did not have an existing fault interface model in this region (Chao *et al.* 2012), so we were not able to project the best slowness of tremor detection back to the source region to determine the tremor location, as was done in Cascadia and other regions (e.g., Ghosh *et al.* 2009).

The dense array also recorded nine tremor bursts (~300 s in total duration, each 20-30 s) triggered by surface waves of the 2011 Mw9.0 Tohoku earthquake. In comparison, the durations of individual ambient tremor events vary from 3-5 minutes to over an hour, although their rate of equivalent radiated seismic energy are 1-3 orders smaller (Figure 10c). In addition, we found an apparent lack of tremor activity for about 20 days following the Tohoku mainshock although some earthquake swarm activity did occur in this gap (Figure 10 and 11). One possible source of contamination is early aftershocks of the teleseismic mainshock, which prevent identification/location of some triggered tremor at Parkfield (Peng *et al.* 2009). However, in our case, we apply a 5-20 Hz filter prior to the array analysis, which should remove most of the teleseismic *P* wave signals from the

24

Tohoku aftershock region. In other words, if tremor did occur in the first 20 days following the Tohoku mainshock, they would likely have been detected by our or the other two WECC techniques. Hence, we argue that the lack of tremor detections following Tohoku is likely real. Similar quiescence of tremor was also observed at the Parkfield-Cholame section of the SAF following large distant earthquakes (Peng *et al.* 2009). We hypothesize that the strong teleseismic event triggered most fault patches that are close to failure (i.e., time advance), resulting in a temporary lack of additional tremor following the large distant events. Interestingly, Pollitz *et al.* (2014) also observed a global quiescence of magnitude > 5.5 earthquake, following a short-term global increase of magnitude > 5.5 earthquake after the 2012/04/11 Mw8.6 Indian Ocean earthquake (Pollitz *et al.* 2012), similar to our observation.

On the other hand, both Chuang *et al.* (2014) and Chao *et al.* (2014) observed that after the 3/4/2010 M_L6.4 Jiashian earthquake located at almost the same location of the LG array, the activities of shallow earthquake swarms (at < 20 km depth) and deep tremor (at 17-34 km depth) increased for about 80 days. Similar increases of tremor activities were found at the Parkfield-Cholame section of the San Andreas Fault following the 2004 Mw6.0 Parkfield earthquake (Nadeau and Guilhem, 2009; Shelly, 2010). In these cases, the moderate earthquakes were very close (i.e., less than 50 km), and hence could change the overall loading rates in the tremor source region, either by static or quasi-static stress changes. Hence, the mechanism of tremor rate change may not be the same as the remotely triggered case in this study.

Several studies have found that systematic migration of ambient tremor, especially in southwest Japan and Cascadia, is common but has different migration speeds. Large-

scale tremor migrates along the subduction-zone strike at about 10 km/day, which tracks the rupture front of slow-slip events (e.g., Obara 2002; Bartlow *et al.* 2011). Sometimes tremor propagates in the opposite direction to the prevailing tremor propagation at speeds of order 100 km/day (e.g., Houston *et al.* 2011). Ghosh *et al.* (2012) propose that asperities at the transition zone, located between the upper locked/seismogenic zone and the lower creeping zone, control tremor generation and rupture propagation, which makes the migration velocity slower inside the asperities and faster in between due to variation in slow-slip velocity along the subduction-zone strike. The average migration speed of some tremor events in this study, at speeds of order of a few tens of km/hour, is similar to fast tremor migration speed along-dip on narrow streaks in Japan and Cascadia (e.g., Shelly *et al.* 2007a; Ghosh *et al.* 2010; Ghosh *et al.* 2012), and both ambient and triggered tremor migration at the Parkfield-Cholame section of the San Andreas Fault (Shelly 2010; Shelly *et al.* 2011). Shelly *et al.* (2007b) propose that the fast migration speed would unlikely accompany with fluid flow but could be due to corrugation in the slip direction, which is similar to a hypothesis of streaks of seismicity on faults (Rubin *et al.* 1999). Because the tremor locations, especially the depth, still have large uncertainties in this region, we could not constrain the fault-dipping angle and determine the relationship between tremor propagation direction and the fault structure.

Our study demonstrates that dense arrays are effective tools for detecting deep tectonic tremor in Taiwan. Therefore, if we can simultaneously install multiple arrays with valid station coverage around tremor sources, such as the Array of Arrays (AofA) in Cascadia (Ghosh 2011), we expect to not only detect more tremor activity but also obtain more accurate tremor locations, especially their depths. Combining with locations of low-

frequency earthquakes (e.g. Tang *et al.* 2013) and earthquake swarms (e.g. Wei Peng, personal communication, 2014) and focal mechanisms of both triggered and ambient tremors, we can better understand the fault motions for generating tremor signals beneath the southern Central Range. Moreover, with the detail spatiotemporal evolution of tremor, we can reveal the relationship between the regular earthquakes and tremor at the bottom of the seismogenic zone at the continental collision environment in southern Taiwan.

APPENDIX A

PARAMETERS

Table A1. Station coordinates of the LG array

Station Name	Latitude (° N)	Longitude (° E)	Elevation (m)
LGA1	23.00288	120.65253	286.2
LGA2	23.00140	120.65128	284.5
LGA3	23.00003	120.65049	280.8
LGA4	22.99858	120.64945	280.0
LGA5	22.99711	120.64859	275.6
LGA6	22.99582	120.64752	274.8
LGB1	23.00207	120.65358	285.0
LGB2	23.00072	120.65254	280.0
LGB3	22.99932	120.65172	282.2
LGB4	22.99770	120.65064	279.4
LGB5	22.99661	120.64997	277.4
LGB6	22.99509	120.64874	273.8
LGC1	23.00149	120.65436	283.8
LGC2	23.00015	120.65353	285.0
LGC3	22.99899	120.65250	279.4
LGC4	22.99726	120.65194	277.0
LGC5	22.99606	120.65107	275.8
LGC6	22.99440	120.64988	273.8
LGD1	23.00091	120.65571	285.6
LGD2	22.99970	120.65502	286.5
LGD3	22.99808	120.65395	284.0
LGD4	22.99654	120.65303	277.2
LGD5	22.99512	120.65201	275.7
LGD6	22.99385	120.65095	275.3
LGE1	23.00014	120.65715	288.3
LGE2	22.99889	120.65603	284.8
LGE3	22.99750	120.65504	280.2
LGE4	22.99615	120.65417	274.5
LGE5	22.99438	120.65304	274.0
LGE6	22.99341	120.65198	275.3
LGF1	22.99948	120.65819	292.0
LGF2	22.99804	120.65691	287.2
LGF3	22.99647	120.65570	287.5
LGF4	22.99549	120.65500	279.8
LGF5	22.99391	120.65415	272.0
LGF6	22.99250	120.65330	275.0

Table A2. Station coordinates of the LD array

Station Name	Latitude (° N)	Longitude (° E)	Elevation (m)
LDA1	23.18536	121.02240	1044.5
LDA2	23.18469	121.02367	1039.3
LDA3	23.18392	121.02463	1030.0
LDA4	23.18324	121.02574	1022.3
LDA5	23.18262	121.02681	1020.8
LDA6	23.18196	121.02752	1015.0
LDB1	23.18582	121.02283	1046.3
LDB2	23.18521	121.02382	1037.8
LDB3	23.18456	121.02508	1029.8
LDB4	23.18367	121.02610	1021.8
LDB5	23.18291	121.02718	1015.0
LDB6	23.18236	121.02814	1015.8
LDC1	23.18634	121.02343	1046.0
LDC2	23.18565	121.02434	1037.3
LDC3	23.18490	121.02544	1024.0
LDC4	23.18418	121.02637	1028.0
LDC5	23.18347	121.02747	1016.7
LDC6	23.18272	121.02851	1016.7
LDD1	23.18673	121.02357	1049.0
LDD2	23.18604	121.02470	1037.0
LDD3	23.18546	121.02580	1027.7
LDD4	23.18461	121.02679	1030.3
LDD5	23.18396	121.02783	1017.3
LDD6	23.18323	121.02882	1018.0
LDE1	23.18709	121.02410	1078.0
LDE2	23.18640	121.02516	1039.0
LDE3	23.18587	121.02596	1034.3
LDE4	23.18504	121.02709	1035.5
LDE5	23.18434	121.02811	1023.3
LDE6	23.18366	121.02912	1016.0
LDF1	23.18759	121.02434	1060.5
LDF2	23.18703	121.02540	1047.0
LDF3	23.18614	121.02645	1036.5
LDF4	23.18551	121.02740	1043.3
LDF5	23.18492	121.02852	1034.3
LDF6	23.18414	121.02949	1059.5

Table A3. Parameters of detected tremor by the combined BBFK-MWGS method

#	Julian Day	Start Hour	Start Min	End Hour	End Min	Duration (min)	Mean BBFK BAZ* (°)	Mean BBFK WN* (1/km)	Mean MWGS BAZ (°)	Mean MWGS CC*
1	43	18	19	18	35	17	47.2	1.06	44.3	0.070
2	44	19	0	19	3	4	70.1	0.68	61.3	0.073
3	44	19	27	20	2	36	79.4	0.87	67.2	0.088
4	44	20	33	20	38	6	37.4	0.97	204.3	0.057
5	45	19	3	19	8	6	45.5	0.73	44.7	0.053
6	45	20	17	20	21	5	43.1	1.26	41.2	0.093
7	46	19	7	19	19	13	49.7	1.10	47.4	0.045
8	46	21	2	21	5	4	43.1	1.35	52.7	0.042
9	49	12	38	13	7	30	84.9	1.00	73.2	0.038
10	50	11	12	11	29	18	87.0	0.89	84.0	0.029
11	53	13	22	13	29	8	67.1	0.97	65.0	0.037
12	56	18	30	18	34	5	101.1	1.16	99.2	0.021
13	56	18	42	18	50	9	58.2	0.97	62.5	0.022
14	56	19	5	19	26	22	78.5	0.85	75.3	0.032
15	56	19	30	19	41	12	75.7	0.84	75.4	0.033
16	57	19	6	19	14	9	48.5	1.16	48.3	0.049
17	64	20	13	20	19	7	100.1	1.35	90.0	0.054
18	66	12	28	12	34	7	73.8	1.06	71.8	0.041
19	66	12	38	12	50	13	84.9	1.06	75.8	0.054
20	69	16	13	16	56	44	60.1	0.69	58.4	0.061
21	69	17	9	17	12	4	59.3	0.77	39.8	0.116
22	69	21	3	21	7	5	62.0	0.68	49.1	0.065
23	89	20	57	21	13	17	52.6	0.99	58.7	0.072
24	89	21	29	21	33	5	67.4	0.97	60.0	0.037
25	89	21	40	21	52	13	83.8	0.84	86.4	0.051
26	90	19	25	19	36	12	84.9	0.94	77.7	0.061
27	90	20	27	20	31	5	68.8	0.68	47.7	0.062
28	93	10	35	10	47	13	84.4	1.06	79.2	0.033
29	113	21	32	21	48	17	80.9	0.90	88.0	0.034
30	116	17	12	17	14	3	46.5	1.26	39.8	0.054
31	116	17	23	17	26	4	49.9	1.06	47.2	0.048
32	118	19	36	19	43	8	51.8	1.11	41.2	0.044
33	119	17	15	17	17	3	32.4	1.06	49.1	0.035
34	119	17	44	18	4	21	78.7	0.97	77.8	0.039
35	120	18	58	19	48	51	79.3	0.83	69.3	0.033
36	120	20	8	20	11	4	87.6	0.97	91.0	0.041
37	121	20	20	20	31	12	50.8	0.90	53.5	0.039
38	123	20	14	20	20	7	31.3	1.06	31.7	0.034
39	128	15	44	15	51	8	76.0	0.82	69.5	0.089
40	130	18	19	18	32	14	62.7	0.87	59.1	0.085
41	133	18	12	18	25	14	71.3	0.87	71.3	0.040
42	135	17	43	18	32	50	82.5	0.95	158.3	0.032
43	137	20	21	21	15	55	79.9	0.85	90.4	0.023
44	146	18	22	18	52	31	74.1	0.87	79.9	0.029
45	149	15	12	15	24	13	101.7	1.06	88.1	0.044
46	149	15	40	15	58	19	96.3	1.08	85.2	0.066
47	149	16	1	16	40	40	64.3	0.91	57.8	0.069
48	149	16	45	16	53	9	86.6	0.82	78.5	0.033

Table A3. Parameters of detected tremor by the combined BBFK-MWGS method (continued)

#	Julian Day	Start Hour	Start Min	End Hour	End Min	Duration (min)	Mean BBFK BAZ* (°)	Mean BBFK WN* (1/km)	Mean MWGS BAZ (°)	Mean MWGS CC*
49	149	16	57	17	15	19	91.8	0.95	83.5	0.063
50	149	17	21	17	39	19	100.3	1.32	90.8	0.067
51	149	18	45	19	12	28	85.8	0.95	76.0	0.110
52	149	19	17	19	37	21	96.0	1.10	89.6	0.082
53	149	19	42	20	42	61	92.4	0.92	75.3	0.106
54	150	18	29	18	35	7	42.5	0.87	43.8	0.178
55	150	19	48	20	12	25	50.4	0.95	43.2	0.117
56	151	18	27	19	10	44	82.5	0.91	71.3	0.095
57	151	20	12	20	27	16	54.4	1.04	48.5	0.125
58	153	21	33	21	42	10	80.2	0.90	76.0	0.049
59	161	15	19	15	24	6	47.5	1.06	64.2	0.037
60	161	16	1	16	20	20	72.8	0.87	74.7	0.034
61	163	18	45	19	7	23	80.2	0.97	79.1	0.037
62	163	19	40	20	11	32	60.4	0.96	65.0	0.046
63	170	16	38	17	1	24	70.9	0.82	60.1	0.085
64	172	17	0	17	10	11	84.9	1.00	65.7	0.055
65	172	17	28	17	37	10	84.3	1.00	69.0	0.057
66	174	15	34	15	45	12	48.0	1.16	45.0	0.105
67	174	15	50	17	9	80	65.6	0.93	60.0	0.084
68	174	18	45	18	51	7	40.5	1.02	39.8	0.084
69	175	16	51	17	25	35	64.7	0.97	66.7	0.091
70	175	17	30	17	54	25	53.2	0.77	50.3	0.085
71	176	14	25	14	33	9	47.7	1.26	45.6	0.074
72	177	18	57	19	2	6	52.6	0.92	50.2	0.103
73	177	19	8	19	19	12	46.2	0.97	49.9	0.056
74	177	19	24	19	30	7	44.5	1.06	44.7	0.073
75	177	20	8	20	27	20	84.2	1.06	72.2	0.052
76	179	18	1	18	8	8	80.9	0.97	77.4	0.048
77	179	18	13	18	49	37	86.2	0.99	80.6	0.056
78	179	19	46	20	5	20	51.8	0.87	50.5	0.068
79	179	20	12	20	18	7	64.7	0.97	67.6	0.054
80	179	21	9	21	12	4	48.5	1.16	45.0	0.056
81	180	19	46	20	10	25	50.4	0.89	50.5	0.057
82	180	20	25	20	45	21	49.3	0.85	50.2	0.086
83	181	20	10	20	15	6	47.5	0.97	45.5	0.153
84	182	21	1	21	10	10	53.3	0.87	59.5	0.027
85	182	21	40	21	43	4	41.8	1.06	54.7	0.048
86	182	22	30	22	48	19	82.5	0.97	91.9	0.023

*BAZ: Back-azimuth; WN: Wavenumber; CC: Cross-correlation Coefficient.

REFERENCES

Aiken, C., Z. Peng, and K. Chao (2013). Tremors along the Queen Charlotte Margin triggered by large teleseismic earthquakes, *Geophys. Res. Lett.* **40**, 1-6, doi: 10.1002/grl.50220I.

Angelier J., J.-C. Lee, H.-T. Chu, J.-C. Hu, C.-Y. Lu, Y.-C. Chan, T.-J. Lin, Y. Font, B. Deffontaines, and Y.-B. Tsai (2001). Le séisme de Chichi (1999) et sa place dans l'orogène de Taiwan, *C. R. Acad. Sci. Paris*, IIa, 333, 1, 5-21.

Bartlow, N. M., S. Miyazaki, A. M. Bradly, and P. Sehall (2011). Space-time correlation of slip and tremor during the 2009 Cascadia slow slip event, *Geophys. Res. Lett.* **38**, L18309, doi: 10.1029/2011GL048714.

Beroza, G. C., and S. Ide (2011). Slow earthquakes and nonvolcanic tremor, *Annu. Rev. Earth Planet. Sci.* **39**, 271-296, doi: 10.1146/annurev-earth-040809-152531.

Boatwright, J., and G. Choy (1986). Teleseismic estimates of the energy radiated by shallow earthquakes. *J. Geophys. Res.*, **91**, B2, 2095-2112, doi: 10.1029/JB091iB02p02095.

Chao, K., Z. Peng, C. Wu, C.-C. Tang, and C.-H. Lin (2012). Remote triggering of non-volcanic tremor around Taiwan, *Geophys. J. Int.* **188**, 1, 301-324, doi: 10.1111/j.1365-246X.2011.05261.x.

Chao, K., Z. Peng, H. Gonzalez-Huizar, C. Aiken, B. Enescu, H. Kao, A. A. Velasco, K. Obara, and T. Matsuzawa (2013). A global search for triggered tremor following the 2011 Mw9.0 Tohoku earthquake, *Bull. Seismol. Soc. Am.* **103**, 2B, 1551-1571, doi: 10.1785/0120120171.

Chao, K., and K. Obara (2014). Triggered tremor in Japan at the inland faulting systems suggesting the existence of background ambient tremor and slow slip, *Science*, to be submitted.

Chao, K., *et al.* (2014). Increasing of tremor rate correlated with slow slip events preceding a nearby Mw6.3 earthquake in Taiwan, to be submitted.

Chuang, L. Y., K. H. Chen, A. G. Wech, T. Byrne, and W. Peng (2014). Ambient tremors in a collisional orogenic belt, *Geophys. Res. Lett.* **41**, 5, 1485-1491, doi: 10.1002/2014GL059476.

Fletcher, J. B., P. Spudich, and L. M. Baker (2006). Rupture propagation of the 2004 Parkfield, California, earthquake from observations at the UPSAR, *Bull. Seismol. Soc. Am.* **96**, 4B, S129-S142, doi: 10.1785/0120050812.

Fletcher, J. B., and L. M. Baker (2010). Analysis of nonvolcanic tremor on the San Andreas fault near Parkfield, CA using U. S. Geological Survey Parkfield Seismic Array, *J. Geophys. Res.* **115**, B10, B10305, doi: 10.1029/2010JB007511.

Frankel, A., S. Hough, P. Friberg, and R. Busby (1991). Observations of Loma Prieta aftershocks from a dense array in Sunnyvale, California, *Bull. Seismol. Soc. Am.* **81**, 5, 1900-1922.

Galgana, G., M. Hamburger, R. McCaffrey, E. Corpyz, and Q. Chen (2007). Analysis of crustal deformation in Luzon, Philippines using geodetic observations and earthquake focal mechanisms, *Tectonophysics* **432**, 63-87, doi: 10.1016/j.tecto.2006.12.001.

Ghosh, A., J. E. Vidale, J. R. Sweet, K. C. Creager and A. G. Wech (2009). Tremor patches in Cascadia revealed by seismic array analysis, *Geophys. Res. Lett.* **36**, 17, L17316, doi: 10.1029/2009GL039080.

Ghosh, A., J. E. Vidale, J. R. Sweet, K. C. Creager, A. G. Wech, and H. Houston (2010). Tremor bands sweep Cascadia, *Geophys. Res. Lett.* **37**, L08301, doi: 10.1029/2009GL042301.

Ghosh, A. (2011). Imaging slow earthquakes in Cascadia using seismic arrays. PhD Dissertation, Department of Earth and Space Sciences, University of Washington, August 2011, pp61-63.

Ghosh, A. (2014). Imaging tremor dynamics on SAF near Parkfield using a mini seismic array, in prep..

Ghosh, A., J. E. Vidale, and K. C. Creager (2012). Tremor asperities in the transition zone control evolution of slow earthquakes, *J. Geophys. Res.* **117**, B10, B10301, doi: 10.1029/2012JB009249.

Goldstein, P., D. Dodge, M. Firpo, and L. Minner (2003). SAC2000: Signal processing and analysis tools for seismologists and engineers, in *In The IASPEI International Handbook of Earthquake and Engineering Seismology, Part B* W. H. K. Lee, KANAMORI, H., Jennings, P.C., and KISSLINGER C. (Editor), Academic Press, London.

Gomberg, J., J. L. Rubinstein, Z. Peng, K. C. Creager, J. E. Vidale, and P. Bodin (2008). Widespread triggering of nonvolcanic tremor in California, *Science* **319**, 173, doi: 10.1126/science.1149164.

Helffrich, G., J. Wookey, and I. Bastow (2013). The seismic analysis code: A primer and user's guide, Cambridge University Press, New York, pp102-106.

Houston H., B. G. Delbridge. A. G. Wech, and K. C. Creager (2011). Rapid tremor reversals in Cascadia generated by a weakened plate interface, *Nat. Geosci.* **4**, 404, doi: 10.1038/NGEO1157.

Huang, B.-S., C.-Y. Wang, D. Okaya, S.-J. Lee, Y.-C Lai, F. T. Wu, W.-T. Liang, and W.-G. Huang (2013). Multiple Diving Waves and Steep Velocity Gradients in the Western Taiwan Coastal Plain: An Investigation Based on the TAIGER Experiment, *Bull. Seismol. Soc. Am.* **103**, 2A, 925-935, doi: 10.1785/0120110047.

Idehara, K., S. Yabe, and S. Ide (2014). Regional and global variations in the temporal clustering of tectonic tremor activity, *Earth Planets Space* **66**, doi:10.1186/1880-5981-66-66.

Kao, H., S. J. Shen, and K.-F. Ma (1998). Transition from oblique subduction to collision: Earthquakes in the southernmost Ryukyu arc-Taiwan region, *J. Geophys. Res.* **103**, B4, 7211-7229, doi: 10.1029/97JB03510.

Kao, H., S.-J. Shan, H. Dragert, G. Rogers, J. F. Cassidy, K. Wang, T. S. Jame, and K. Ramachandran (2006). Spatial-temporal patterns of seismic tremors in northern Cascadia, *J. Geophys. Res.* **111**, B3, B03309, doi: 10.1029/2005JB003727.

La Rocca, M., D. Galluzzo, S. Malone, W. McCausland, G. Saccorotti, and E. Del Pezzo (2008). Testing small-aperture array analysis on well-located earthquakes, and application to the location of deep tremor, *Bull. Seismol. Soc. Am.* **98**, 2, 620-635, doi: 10.1785/0120060185.

Nadeau, R. M., and D. Dolenc (2005). Nonvolcanic tremors deep beneath the San Andreas fault, *Science* **307**, 389, doi: 10.1126/science.1107142.

Nawab, S. H., F. U. Dowla, and R. T. Lacoss (1985). Direction determination of wideband signals, *Acoustics, Speech and Signal Processing, IEEE Transactions on* **33**, 5, 1114-1122, doi: 0096-3518/85/1000-1114.

Nishiwaza, A., K. Kameda, and M. Okawa (2009). Seismic Structure of the Northern End of the Ryukyu Trench Subduction Zone, Southeast of Kyushu, Japan, *Earth, Planets and Space* **61**, 8, e37–e40, doi: 10.1186/BF03352942.

Obara, K. (2002). Nonvolcanic deep tremor associated with subduction in southwest Japan. *Science* **296**, 1679–1681, doi: 10.1126/science.1070378.

Peng, Z., and K. Chao (2008). Non-volcanic tremor beneath the Central Range in Taiwan triggered by the 2001 Mw7.8 Kunlun earthquake, *Geophys. J. Int.* **175**, 2, 825-829, doi: 10.1111/j.1365-246X.2008.03886.x.

Peng, Z., J. E. Vidale, A. G. Wech, R. M. Nadeau, and K. C. Creager (2009). Remote triggering of tremor along the San Andreas Fault in central California, *J. Geophys. Res.* **114**, B00A06, doi: 10.1029/2008JB006049.

Peng, Z., and J. Gomberg (2010). An integrated perspective of the continuum between earthquakes and slow-slip phenomena, *Geophys. Res. Lett..* **3**, 599 - 607, doi: 10.1038/ngeo940.

Peng, Z., H. Gonzalez-Huizar, K. Chao, C. Aiken, B. Moreno, and G. Armstrong (2013). Tectonic tremor beneath Cuba triggered by the Mw8.8 Maule and Mw9.0 Tohoku-Oki earthquakes, *Bull. Seismol. Soc. Am.* **103**, 1, 595-600, doi: 10.1785/0120120253.

Pollitz, F. F., R. S. Stein, V. Sevilgen, and R. Bürgmann (2012). The 11 April 2012 east Indian Ocean earthquake triggered large aftershock workwide, *Nature* 490, 250-253, doi:10.1038/nature11504.

Pollitz, F. F., R. Bürgmann, R. S. Stein, and V. Sevilgen (2014). The profound reach of the 11 April 2012 M 8.6 Indian Ocean Earthquake: Short-term global triggering followed by a longer-term global shadow, *Bull. Seismol. Soc. Am.* **104**, 2, 972–984, doi: 10.1785/0120130078.

Rogers, G., and H. Dragert (2003). Episodic tremor and slip on the Cascadia subduction zone: The chatter of silent slip, *Science* **300**, 1942-1943, doi: 10.1126/science.1084783.

Rost, S., and C. Thomas (2002). Array seismology: Methods and applications, *Rev. Geophys.* **40**, 3, 2-1–2-27, doi: 10.1029/2000RG000100.

Rubin, A. M., D. Gillard, and J.-L, Got (1999). Streaks of microearthquakes along creeping faults, *Nature* **400**, 635-641, doi:10.1038/23196.

Ryberg, T., Ch. Haberland, G. S. Fuis, W. L. Ellsworth, and D. R. Shelly (2010). Locating non-volcanic tremor along the San Andreas Fault using a multiple array source imaging technique, *Geophys. J. Int.* **183**, 3, 1485-1500, doi: 10.1111/j.1365-246X.2010.04805.x.

Shelly, D. R., G. C. Beroza, and S. Ide (2007a). Non-volcanic tremor and low frequency earthquake swarms, *Nature* **446**, 305-307, doi:10.1038/nature05666.

Shelly, D. R., G. C. Beroza, and S. Ide (2007b). Complex evolution of transient slip drived from precise tremor loctaions in western Shikoku, Japan, *Geochem. Geophys. Geosyst.* **8**, Q10014, dio:10.1029/2007GC001640.

Shelly, D. R., W. L. Ellsworth, Tr. Ryberg, C. Haberland, G. S. Fuis, J. Murphy, R. M. Nadeau, and R. Bürgmann (2009). Precise location of San Andreas Fault tremors near Cholame, California using seismometer clusters: Slip on the deep extension of the fault?, *Geophys. Res. Lett.* **36**, L01303, doi: 10.1029/2008GL036367.

Shelly, D. R., and J. L. Hardebeck (2010). Precise tremor source locations and amplitude variations along the lower-crustal central San Andreas Fault, *Geophys. Res. Lett.* **37**, L14301, doi: 10.1029/2010GL043672.

Shelly, D. R. (2010). Migration tremors illuminate complex deformation beneath the seismogenic San Andreas fault, *Nature* **463**, 648-653, doi:10.1038/nature08755.

Shelly, D. R., Z. Peng, D. P. Hill, and A. Chastity (2011). Triggered creep as a possible mechanism for delayed dynamic triggering of tremor and earthquakes, *Nature Geosci.* **4**, 384-388, doi: 10.1038/ngeo1141.

Shin, T.-C., C.-H. Chang, H.-C. Pu, H.-W. Lin, and P.-L. Leu (2013). The geophysical database management system in Taiwan, *Terr. Atmos. Ocean. Sci.* **24**, 1, 11-18, doi: 10.3319/TAO.2012.09.20.01(T).

Tang, C.-C., Z. Peng, K. Chao, C.-H. Chen, and C.-H. Lin (2010). Detecting low-frequency earthquakes within non-volcanic tremor in southern Taiwan triggered by the 2005 Mw8.6 Nias earthquake, *Geophys. Res. Lett.* **37**, L16307, doi: 10.1029/2010GL043918.

Tang, C.-C., Z. Peng, C.-H. Lin, K. Chao, and C.-H. Chen (2013). Statistical properties of low-frequency earthquakes triggered by large earthquakes in southern Taiwan, *Earth Planet. Sci. Lett.* **373**, 1-7, doi: 10.1016/j.epsl.2013.04.039.

Tsai, Y.-B. (1986). Seismotectonics of Taiwan, *Tectonophysics* **125**, 1, 17-37, doi: 10.1016/0040-1951(86)90005-3.

Ueno, T., T. Maeda, K. Obara, Y. Asano, and T. Takeda (2010). Migration of low-frequency tremors revealed from multiple-array analyses in western Shikoku, Japan, *J. Geophys. Res.* **115**, B00A26, doi: 10.1029/2008JB006051.

Wech, A. G., and K. C. Creager (2008). Automated detection and location of Cascadia tremor, *Geophys. Res. Lett.* **35**, 20, doi: 10.1029/2008GL035458.

Wech, A. G. (2010). Interactive tremor monitoring, *Seismol. Res. Lett.* **81**, 4, 664-669, doi: 10.1785/gssrl.81.4.664.

Wech, A. G., C. M. Boese, T. A. Stem, and J. Townend (2012). Tectonic tremor and deep slow slip on the Alpine Fault, *Geophys. Res. Lett.* **39**, L10303, doi: 10.1029/2012GL051751.

Wu, Y., C.-H. Chang, L. Zhao, and T.-L. Teng (2008). A comprehensive relocation of earthquakes in Taiwan from 1991 to 2005, *Bull. Seismol. Soc. Am.* **98**, 3, 1471-1481, doi: 10.1785/0120070166.

Wu F. T., H. Kuo-Chen, and K. D. McIntosh (2014). Subsurface image, TAIGER experiments and tectonic models of Taiwan, *J. Asian Earth Sci.* **90**, 173-208, doi: 10.1016/j.jseaes.2014.03.024.

Yu, S., H.-Y. Chen and L.-C. Kuo (1997). Velocity field of GPS stations in the Taiwan area, *Tectonophysics* **274**, 41-59, doi: 10.1016/S0040-1951(96)00297-1.